Role of crustal fluids and thermo-mechanical structure for lower crustal seismicity: the Gargano Promontory (southern Italy)

Alessio Lavecchia[a,b,*], Marilena Filippucci[a], Andrea Tallarico[a], Giulio Selvaggi[b], Gianpaolo Cecere[b], Sierd Cloetingh[c]

[a]*Dipartimento di Scienze della Terra e Geoambientali, Università di Bari - Aldo Moro, Bari, Italy*
[b]*Istituto Nazionale di Geofisica e Vulcanologia, Centro Nazionale Terremoti, Rome, Italy*
[c]*Department of Earth Sciences, Utrecht University, Utrecht, The Netherlands*

Abstract

Several regions around the globe are characterized by a seismically active lower crust, at depths where lithological, thermal and rheological conditions suggest stress release by ductile flow. The Gargano Promontory (GP, southern Italy) is an example where a recently installed seismic network has recorded an intense seismic activity at depths between 20 and 30 km, i.e. in the lower crust. We analyze a possible mechanism controlling the distribution of seismicity in the GP to identify the factors that make the lower crust seismically active. To this aim, we construct a thermo-rheological model of a layered continental crust, calibrated on the basis of geometrical, lithological and thermal constraints. The model takes into account a multiphase crustal lithology, the presence of fluids in the crystalline basement, lateral variations of geotherm and stress field.

The numerical simulations show that the presence of fluids is a key factor controlling the cluster of seismicity in the lower crust. Moreover, the

*Corresponding author

presence of water in the upper crystalline basement and sedimentary cover provides a plausible explanation for upper crustal seismicity in a zone of very high heat flow SW of the GP. The distribution of the seismicity is probably affected by the composition of the crystalline basement, with mafic bodies injected into the crust during the Paleocene magmatic phase that affected the Mediterranean region. Our findings suggest that the presence of hydrous diapiric upwelling(s) in the upper mantle can feed a deep fluid circulation system, inducing lower crustal seismicity.

Keywords: Lower crust, Seismology, Rheology, Geotherm, Numerical modeling, Gargano Promontory (southern Italy).

1. Introduction

The continental lower crust has historically been considered a weak layer, transferring stresses between the brittle upper crust and the lithospheric mantle via ductile flow (Burov, 2011). In this framework, the lack of seismicity is one of the main features of the lower crust. Earthquake hypocenters are not frequently detected in the lower crust and the correlation between depth of crustal seismicity, temperature and rock deformation mechanisms has led to the common view that the lower continental crystalline basement is ductile (Chen and Molnar, 1983). This is true in many continental areas, especially where the geothermal gradient is particularly high, as for instance in the Pannonian Basin of central Europe (Cloetingh and Burov, 1996; Lenkey et al., 2002). On the other hand, recent studies suggest that a strong lower crust is present in many areas (e.g. Maggi et al., 2000) and seismicity nucleated in the continental lower crust is also observed in several locations around the

globe (e.g. Simpson, 1999), including some major rift zones, such as the East African rift (Shudofsky et al., 1987), Baikal rift (Déverchère et al., 2001), Rhine rift (Deichmann, 1992) and the Dead Sea rift (Aldersons et al., 2003; Salamon et al., 2003).

The causes behind the nucleation of earthquakes in the lower crust are still a matter of an intense debate (e.g. Simpson, 1999; Campbell et al., 2020). The most common proposed mechanisms so far include thermal-runaway plastic instability, dehydration reactions with subsequent increase in fluid pressure, local stress redistribution, transient high differential stress values and eclogitisation reactions (Campbell et al., 2020, and references therein).

Fluid presence and circulation in the lower crust is one of the mechanisms that may promote seismicity (e.g. Audin et al., 2002; Gardonio et al., 2018; Benson et al., 2020, and references therein). In this context, it is of particular importance to distinguish between short-term and long-term effects of fluids on host rocks. The former is mostly mechanical and the presence of interconnected fluid phases decreases the shear stress needed to produce rock failure, favoring the likelihood of faulting and sliding (e.g. Ranalli, 1995; El Hariri et al., 2010; Van Dinther et al., 2013). On the other hand, host rocks can be subjected to effects of hydrolythic weakening and therefore their strength can be significantly reduced (Tullis and Yund, 1989; Girard et al., 2013). Furthermore, fluids can exert a long term chemical effect by triggering metamorphic reactions and producing rheologically weaker rocks where deformation will mostly occur by viscous creep (e.g. Jamtveit et al., 2019; Wang et al., 2020). Therefore, the study of fluid-crust interaction is pivotal to assess the seismic hazard in seismically active regions. In addition, rock-

fluids in the continental crust can form pore networks along grain edges and fluid percolation by either porous flow or surface energy-driven infiltration can affect electrical and thermal properties in the lower crust (e.g. Watson and Brenan, 1987). These mechanisms are localized within shear zones in the lower crust, where creep cavitation and subgrain rotation recrystallization during mylonite formation gives rise to cavities (Menegon et al., 2015; Gilgannon et al., 2020).

One of the regions where intense seismicity has been detected in the lower crust is the Gargano Promontory (GP) of southern Italy. The area is historically characterized by earthquakes with magnitude $M_w < 6.5$, some of them associated with two main E-W fault systems: the Mattinata Fault and the Tremiti Fault (Del Gaudio et al., 2007). Until 2013, only two seismic stations of the Italian National Seismic Network (international code IV) were operating on the GP (MSAG, SGRT) (Fig. 1A). As a consequence, a high degree of inaccuracy was unavoidable in the detection and localization of the GP earthquakes. The seismic coverage of the region was largely improved with the installation of the OTRIONS seismic network (international code OT) in 2013, allowing the detection of micro-earthquakes and a significant expansion of the seismic database (Filippucci et al., 2021b). Stations of OT network and of IV network co-work to form the Gargano Seismic Network (GSN in Fig. 1A).

Recent studies of the recorded seismicity (Filippucci et al., 2019a,b, 2021a,b; Miccolis et al., 2021) highlight an intense micro-earthquake activity in the whole GP at depths greater than 20 km (Fig. 1B). Hypocenters gently deepen towards the NE reaching depths of about 30 km (Fig. 1B). Focal

mechanisms of earthquakes occurring in the NE part of the GP show thrust faulting kinematics (Filippucci et al., 2020; Miccolis et al., 2021). Conversely, seismic activity SW of the GP is markedly shallower, with a maximum depth around 10 km and affects an area located along the Candelaro Fault (CF in Fig. 1B), with focal mechanisms showing normal faulting kinematics.

A very high surface heat flow is measured in the CF area where this shallow seismicity is observed, with values that may exceed 100 mW m^{-2} (Fig. 1A). In this area the presence of water in crustal rocks has been observed (Tripaldi, 2020). Therefore, the high surface heat flow has been attributed to thermal conductivity increase and heat transport at shallow depth in the sedimentary cover due to fluid circulation (Della Vedova et al., 2001). On the other side, fluid presence at greater depth has not been unambiguously identified (Tripaldi, 2020).

A first attempt to study the GP crustal rheology was conducted by Dragoni et al. (1996) with an analytical 1D model. In this study a temperature-dependent viscosity was implemented and a transcurrent stress field and an average surface heat flow of 60 mW m^{-2} were adopted for the area. Recently this model was updated by Filippucci et al. (2019b), utilizing the heat flow map of Della Vedova et al. (2001) and subdividing the GP area in two different surface heat flow zones.

In this paper we propose a numerical 2D thermo-rheological model, taking into account the effects of thermal, lithological and tectonic variations, both lateral and vertical, on rock strength under dry and wet conditions. This approach allows us to evaluate the rheological effect of fluid presence and consequences for seismicity and surface heat flow. With our model we

calculate thermal structure and brittle-ductile strength distribution in 2D, adopting the GP as a test bed. With this study, we aim to better understand the main parameters controlling the distribution of seismicity, as well as their interaction. We show that the seismic clustering at lower crustal depths is probably triggered by high pore fluid pressure, in combination with the presence of mafic bodies injecting the crystalline basement.

2. Tectonic framework

The GP is part of the Adria platform (Fig. 1A), a region that constitutes the foreland-foredeep area of three orogenic systems: Alps to the N, Apennines to the W and Dinarides to the E (e.g. D'Agostino et al., 2008, and references therein). During the Eurasia-Africa convergence, the Adria plate acted as an indenter (Aliaj, 2006; Stein and Sella, 2006) and moved coherently with the African plate at least until late Miocene (Babbucci et al., 2004). Subsequently, the development of the westward Anatolian-Aegean-Balkan system resulted in decoupling of Adria from the Africa plate and a clockwise rotation of Adria with respect to Eurasia. As a consequence of this event, Adria movement changed to a counterclockwise rotation during late Pliocene to early Pleistocene, due to the plate collision with the southern parts of the Apennines (D'Agostino et al., 2008, and references therein). Although the current plate configuration in the Adria region is still controversial, recent studies suggest that Adria is today separated in two blocks along the Gargano-Dubrovnik lineament (Fig. 1A) (Oldow et al., 2002). Seismological and geodetic studies point out that at present day the Apulian sector moves independently from northern Adria, in a framework where Apu-

lia moves coherently with the Ionian Sea and the Hyblean block (D'Agostino et al., 2008). The separation between Adria and Africa has been identified along the Apulian Escarpment (e.g. Battaglia et al., 2004) or alternatively in a region of diffuse deformation in the Ionian Sea (Stein and Sella, 2006).

In this framework, the GP represents a region located at the boundary between the northern and southern Adriatic subplates. The GP represents the most elevated part of the Apulian foreland, with maximum height around 1000 m, and is structured in an elongated anticline affected by faults trending NW-SE, E-W and subordinately NE-SW (Argnani et al., 2009). The nature and development sequence of the GP fault system is still a matter of debate. Some studies highlight the role of strike-slip motion along E-W major faults, e.g. the Mattinata and Rignano faults (Brankman and Aydin, 2004). Other studies emphasise the contribution of compressive deformation related to the stress field from the Dinarides, with direction N-S and NE-SW (e.g. Bertotti et al., 1999). The most recent sediments occurring in the GP are shallow water marine deposits of late Miocene age, exposed today at 100 m height above sea level. Therefore, the onset of uplift in the region might have started during late Miocene to Pliocene, with a minimum estimated uplift rate 0.1 mm/yr (Bertotti et al., 1999, and references therein). Two superimposed extensional phases can be observed in the GP. The first one is characterized by NE-SW extension, probably occurring during late Cretaceous (Winter and Tapponnier, 1991), whereas the second was directed NW-SE during Paleogene (Argnani et al., 2009). Extension precedes a phase of compression during late Miocene-Pliocene, both onshore and offshore (Bertotti et al., 1999; Brankman and Aydin, 2004). The compressive

phase is coupled with thrusting along NW-trending, SW-verging high angle faults, and reactivation of pre-existing normal faults (Bertotti et al., 1999; Brankman and Aydin, 2004).

At present day, low to moderate seismicity is recorded in Apulia. On the other hand, the GP historical seismicity is much more intense, with about 15 earthquakes characterized by $M_W > 5.5$ since 1361 (Rovida et al., 2019). The hypocentral depths and other features of the largest earthquakes in the region show that the present-day stress field affecting the basement of the GP is mostly compressional. In addition, clusters of shallow extensional earthquakes have been recently detected SW of the promontory (Heidbach et al., 2019; Filippucci et al., 2020; Miccolis et al., 2021).

The GP was affected by anorogenic magmatism during Paleocene. This magmatic phase did not only occur in the GP, but is rather widespread throughout the Mediterranean and surrounding regions and is commonly referred as the Circum-Mediterranean Anorogenic Cenozoic Igneous (CiMACI) province (Lustrino and Wilson, 2007, and references therein). Gravimetric studies detected positive anomalies in the entire Apulian area (Tassis et al., 2013), which have been interpreted as resulting from the emplacement of mafic igneous bodies at various depths in the crust (Loddo et al., 1996). The GP igneous bodies crop out in Punta delle Pietre Nere (Fig. 1A), intruding upper Triassic sedimentary successions, and consist of amphibole-bearing alkali-gabbros and alkali-syenite rocks of age 58 and 62 Ma respectively, with lamprophyric affinity (Mazzeo et al., 2018, and references therein). The gabbroic body contains subordinated pyroxenite and is interpreted as part of a more extensive layered intrusion (De Fino et al., 1981).

Due to major compositional differences (Mazzeo et al., 2018) and the long time span between the emplacement of gabbros and alkali-syenites (Bigazzi et al., 1996), it is unlikely that there is a genetic link between the two igneous bodies. These rocks show geochemical affinity with ocean island basalts series and an intermediate composition between depleted mantle material, enriched material and Hi-μ sources, with particularly pronounced latter one. A recent study (Mazzeo et al., 2018) suggests that these rocks might derive from partial melting of an amphibole-rich lithospheric mantle at depths exceeding 70-90 km and pressure of 2.5-3.5 GPa, corresponding to the spinel-garnet transition depth. The geodynamic conditions leading to partial melting are still a matter of debate. However, there exists a general consensus on mantle plume components characterizing these rocks (e.g. Lustrino and Wilson, 2007). Given the small volume and short duration of magmatic activity in the GP, a mantle diapir impinging the area may have small size and/or low potential temperature, making its detection difficult (e.g. Kuritani et al., 2017; Koptev et al., 2021).

These factors have been taken into account in the heterogeneous stress field and in the lithological composition adopted in our numerical simulations.

3. The model

The investigated crustal section has a length of 60 km and width of 32 km (Fig. 2) with SW-NE orientation following the A-B lineament (Fig. 1B). The seismicity distribution follows a vertical trend SW of the GP and a deep sub-horizontal distribution toward NE.

We test the hypothesis that seismicity in the GP can be related not only

to the interactions between lithology and stress conditions in the region, but also to fracturing and fluid presence. Therefore, we include in the model the presence of zones where fracking and fluids occur (light blue zones in Fig. 2), taking into account their effect on rock thermal and rheological parameters (pore fluid factor λ, cohesion factor S, thermal conductivity k_i (Table 1)). The size and shape of these zones are based on hypocenter locations in the GP (Fig. 1). The crustal section consists of 6-layers, each characterized by different lithologies and corresponding different thermal and mechanical parameters. Thickness and petrological parameters of each layer correspond to crustal characteristics of the Adria plate and, where possible, to the constraints from geophysical data for the GP. The 3 top layers represent the sedimentary cover of the Adria crust, whereas the 3 layers underneath represent the crystalline basement. The sedimentary cover overlays a Hercynian basement that has been documented for the Apulian margin in a number of previous studies (e.g. Schenk, 1981). Further information on the petrological characteristics of the GP crust is available in Appendix A, while minerals percentage for each layer and corresponding rheological parameters are specified in Table 2. The lithologies constituting the crustal layers are given in Amato et al. (2014) and Morsili (2016) while the relative parameters are given in Table 1.

We construct a steady-state 2D thermal model providing the temperature field and surface heat flow in a multilayered crust (see Fig. 2 for details). The temperature $T(x, z)$ is calculated, taking into account the characteristics

of each i-th layer, by the steady state heat equation:

$$\nabla \cdot \left(\frac{k_i}{\rho C_{pi}} \nabla T \right) = H \tag{1}$$

where k_i is the thermal conductivity for each i-th layer and is equal to k_{di} or $k_{wi} = 3k_{di}$ depending on dry or wet condition respectively (Clauser and Huenges, 1995, and references therein), ρ is the density, C_{pi} is the specific heat at constant pressure and H is the radiogenic heat production, given by:

$$H(z) = H_0 \exp\left(-\frac{z}{D}\right) \tag{2}$$

where H_0 is the radiogenic heat production at the Earth's surface, D is the characteristic depth and z is the depth. The density $\rho(x, z)$ is temperature-dependent, according to the equation:

$$\rho(x, z) = \rho_{0i}\{1 - \alpha[T(x, z) - T_0]\} \tag{3}$$

where ρ_{0i} is the density of rocks at surface temperature and pressure and α is the thermal expansion coefficient for crustal rocks. $T(x, z)$ is calculated with the boundary conditions $T(x, 0) = T_0$ at the surface and $T(x, z_6) = T_b$ at the base. Temperature at the base of continental crust shows a wide range of variations (e.g. Pasquale et al., 1990; Schutt et al., 2018; Gruber et al., 2021). Two values of T_b (450 and 500 °C) have been adopted to test the sensitivity of the models to base temperatures. These values are chosen to best fit the calculated heat flow at surface with the surface heat flow values measured in the GP region (Della Vedova et al., 2001).

We numerically solved eq. (1) by using FreeFEM++ (Hecht, 2012) a software specifically designed to solve systems of partial differential equations (PDEs). This software is based on the finite element method to solve

linear and nonlinear multi-equation systems in an automated framework, and provides mesh generators and easy geometric input. The mesh adopted for the model is composed of triangular elements and it is based on the Delaunay-Voronoi algorithm. This ensures the minimization of sliver triangles in the model domain, and therefore improves the accuracy and speed of the PDEs solver. Several element sizes have been tested to obtain an accurate solution and a fast calculation speed. We have verified that a valid choice is represented by a mesh built from elements with edges of 250 m around the domain boundaries. Therefore, this size has been adopted for all simulations. The solver implemented is the generalized minimal residual method, with an imposed minimal residual $\zeta = 10^{-6}$.

The heat flow $\mathbf{q}(x, z)$ is computed by:

$$\mathbf{q}(x, z) = k_i \nabla T(x, z) \tag{4}$$

and its surface vertical component $q_0(x, 0)$ is compared with the surface heat flow map (Della Vedova et al., 2001) along the A-B lineament (Fig. 1B) in order to validate the geothermal model.

We adopt a rheological model to evaluate the brittle-ductile behavior of the crustal section. The differential shear stress $\Delta\sigma_m(x, z)$ for faulting, which is the fault strength, is calculated by adopting the Coulomb-Navier criterion (Yin and Ranalli, 1992):

$$\Delta\sigma_m(x, z) = \frac{2\kappa\rho g z(1 - \lambda) + 2S}{(\kappa^2 + 1)^{\frac{1}{2}} \pm \kappa} \tag{5}$$

where κ is the coefficient of steady sliding friction, g is the acceleration of gravity, λ is the pore fluid coefficient and corresponds to λ_d or λ_w depending on dry or wet conditions respectively, S is the cohesion coefficient and

corresponds to S_u or S_f depending on unfractured or fractured conditions respectively. The values of S and λ are independent on lithology and vary according to either dry or wet conditions in the model (Table 2). We take into account the drop of $\Delta\sigma_m$ due to fractures through the coefficient S and due to fluid presence through the coefficient λ. Fracturing and faulting can induce porosity and subsequently determine a loss of cohesion, favouring a brittle regime. The stress field pattern (Miccolis et al., 2021) shows a compressive regime for the NE part of the GP, whereas evidence of an extensive regime exists for the SW part of the GP (Filippucci et al., 2020). The deformation regime exerts a primary control over rock strength in geodynamically active regions (e.g. Neely and Stein, 2021). Therefore, compressional/extensional deformation is modeled by introducing a $\pm$ operator in eq. (5) (+ for extension, - for compression).

Under the assumption of power-law creep, the maximum tectonic differential shear stress $\Delta\sigma_M(x,z)$ is calculated by adopting the Dorn equation (Gerya, 2009; Filippucci et al., 2019b):

$$\Delta\sigma_M(x,z) = \left(\frac{\dot{\varepsilon}}{A_i}\right)^{\frac{1}{n_i}} \exp\left(\frac{Q_i}{n_i RT}\right) \tag{6}$$

where $\dot{\varepsilon}$ is the strain rate, n_i is the exponent of the rheological power-law creep, A_i is the Dorn parameter, Q_i is the activation energy, R is the gas constant and T is the absolute temperature. Each lithology is polymineralic and each mineral composing the crust layers has distinct values of rheological parameters. Therefore, the parameters of minerals and their volume percentage are used to calculate A_i, n_i and Q_i for each layer. The details of the averaging method are fully described in Ji et al. (2003). The strain

rate $\dot{\varepsilon} = 10^{-14}$ s^{-1} is an average value for geodynamically active areas (e.g. Ranalli, 1995; Fagereng and Biggs, 2019).

The rheological behavior of the crust can be defined by the minimum differential stress

$$\sigma_d(x,z) = \min[\Delta\sigma_M(x,z); \Delta\sigma_m(x,z)] \tag{7}$$

representing the crustal strength. For $\sigma_d(x,z) = \Delta\sigma_M(x,z)$ the rheological behavior is brittle; while for $\sigma_d(x,z) = \Delta\sigma_m(x,z)$ the rheological behavior is ductile. As a consequence the crustal rheology can be represented by the step function

$$Rh(x,z) = \begin{cases} 0, & \text{if} \quad \sigma_d = \Delta\sigma_M(x,z) \\ 1, & \text{if} \quad \sigma_d = \Delta\sigma_m(x,z) \end{cases} \tag{8}$$

4. Results

The parameters adopted in each simulation case are summarized in Table 2A. In our simulations the crust is composed of layers with thickness th_i and bottom depth z_i. The layer thickness is kept constant in all the simulations, except for the case D (Table 2A). In order to evaluate the effect of parameters on rheology we adopt four different geotherms, assuming two different values of T_b and either dry or wet conditions in correspondence of low cohesion zones (light blue area of Fig. 2). For each geotherm we test the effect of variations in cohesion factor S, pore fluid factor λ, thickness of the crystalline basement layers (th_4, th_5, th_6) and petrological composition on σ_d and Rh. The results of the model are shown in Figs. 3-6. A flow chart in Appendix B (Fig. B.1) summarizes the procedure followed for the model development and the obtained results.

4.1. Crustal strength σ_d

When rocks are subjected to compression, the maximum value of σ_d in the sedimentary cover is constant independently on the investigated setting, with $\sigma_d \approx 360$ MPa. Differently, in the same layer σ_d is significantly lower when extension occurs and is subjected to large variations. In unfractured, dry conditions (case A), $\sigma_d \approx 150$ MPa, whereas $\sigma_d \approx 60$ MPa in regions where the presence of fractures leads to a cohesion drop (case B) and $\sigma_d \approx 20$ MPa in wet conditions (cases C-G). The strength σ_d calculated in the crystalline basement is significantly lower than in the sedimentary cover in compressive areas. In the basement, the calculated maximum value of σ_d is less than 260 MPa (cases A and B) and further decreases to 140 MPa when fluids are present in the lower crust (case C). A rise in σ_d takes place when a colder geotherm is adopted (cases D-G). It results in σ_d between 160 MPa when either a granodiorite or metasedimentary middle crust is implemented (cases E and G), and 220 MPa when we investigate a thicker lower crust (case D). One exception is when mafic rocks are present in the basement (case F). In this simulation, σ_d can exceed 500 MPa in a thin layer at the top of the injected middle crust.

4.2. Crustal rheology Rh

All simulations show a brittle behavior for most of the sedimentary cover in both compressional and extensional settings. The brittle-ductile transition is located at a depth of 6 km and its depth variations, due to changes in the geotherm and compressional-to-extensional setup, are negligible. The crystalline basement retains a ductile behavior in the absence of fluids, regardless of the adopted geotherm. This can be promptly observed in unfractured, dry

conditions (case A). Low values of cohesion (case B) in the extensional domain can lead to a deepening of the brittle-ductile transition to a depth of 10 km and the appearance of thin brittle layers deeper in the crystalline basement. However, the domain subjected to compression is totally unaffected by low cohesion.

The presence of fluids exerts a more profound effect on the crustal rheology and can trigger the appearance of thick brittle layers in the previously ductile crystalline basement. In the lower crust, fluids cause an increase in thermal conductivity and, therefore, variations in geotherm (case C). This is combined with high values of the pore fluid factor and leads to the appearance of well-developed brittle regions where the crust is subjected to extension. In contrast, where compression occurs and $T_b = 500°C$, the crust is only slightly affected by fluids. Consequently, the ductile behavior is still retained, except for a thin brittle layer marking the boundary between middle and lower crust. In order to test the sensitivity of the model to different geotherms, a colder temperature field has been implemented, based on a temperature at the bottom of the crust $T_b = 450\,°C$ (geotherm III and IV, cases D-G). In the resulting simulations the combined effect of high thermal conductivity, high pore fluid factor, low cohesion and low temperatures leads to the appearance of thick brittle layers in the extensional domain of the model (case D). These layers affect both the middle and the lower crust, with depths between 20 km and 30 km. On the other hand, where compression occurs only the lower crust shows a brittle behavior in a 4 km thick layer, whereas the middle crust rheology remains unaffected by fluid presence. The brittle region within the crystalline basement is well defined, but still too thin

to be compatible with the presence of the seismogenic layer at the base of the GP crust. Therefore, we tested the sensitivity of this region's thickness to variations in crustal composition and lower crust thickness. When the lower crust extends from a depth of 20 km down to the base of the model, it overlaps the region of fluid presence (case C). As a result, the brittle layer has a thickness of 8-10 km, with its upper boundary coinciding with the middle-lower crust boundary. The presence of magmatic bodies in the GP has been taken into consideration by carrying out simulations where mafic rocks constitute part of the crystalline basement, up to 35 % vol (cases F and G). There is a high degree of uncertainty on the characteristics of the mafic rocks intruding the Apulian basement. However, reflective magmatic bodies have been detected at mid-crustal depth in previous seismic studies (Finetti and Del Ben, 2005), while a thick band of parallel reflectors has been detected in the lower crust and interpreted as layering (Amato et al., 2014). For these reasons, the mafic component has been added at middle and lower crust depth. In addition, simulations where mafic rocks are also present in the upper crust are included in Appendix C (Fig. C.1). All these simulations are characterized by a significant increase in rock strength, with values exceeding 500 MPa in the middle crust (case F). Moreover, brittle behavior is no longer confined within the lower crust, but now it also affects the middle crust, in both the compressional and extensional domains, in a similar fashion to the layered, "corset-like" model proposed by Meissner and Kern (2008). As a consequence, the simulated brittle layer can exceed a thickness of 10 km. On the other hand, a metasedimentary middle crust composition (case G) still retains a ductile rheology, even if partly constituted by mafic

rocks. Therefore, in this simulation the brittle layer is significantly thinner than the preceding cases and does not exceed a thickness of 6 km. Further simulations have been carried out to test the sensitivity of rheology variations to fluid presence and strain rate (Fig. C.1 in Appendix C). These additional simulations confirm the pivotal role of fluids to promote a brittle rheological behavior at depth in the crust, even when mafic rocks are present in the entire crystalline basement or the deformation rate is very high.

4.3. Effects of geotherms on surface heat flow q_0

Fluid presence has a significant effect on the thermal state of the crust. Therefore, by influencing the values of thermal conductivity of rocks, fluids also affect the heat flow in the crust. In areas where water is not present, we calculate a value of surface heat flow $q_0 \approx 30\,\mathrm{mW\ m^{-2}}$ (geotherm I). Differently, the presence of fluids at the bottom of the model leads to higher thermal conductivity and higher temperatures in the fluid rich layer (geotherm II). This is accompanied by a value of surface heat flow $q_0 \approx 40\,\mathrm{mW\ m^{-2}}$. When a region rich in fluids covers the whole crustal thickness, the increase in thermal conductivity is significant enough to determine a large rise in surface heat flow, with $q_0 \approx 110$ mW m^{-2} when $T_b = 500\,^{\circ}\mathrm{C}$ (geotherm II), and $q_0 \approx 100$ mW m^{-2} when $T_b = 450\,^{\circ}\mathrm{C}$ (geotherms III and IV). This effect is partly mitigated by lower values of thermal gradient, especially where the horizontal and vertical fluid-rich intervals intersect.

5. Discussion

In the above, we investigated the effect of fluid presence, thermal state, lithology, fractures and heterogeneous tectonic stress regime on crustal rhe-

ological properties in the GP, comparing our results with the recorded seismicity distribution and surface heat flow measured in the area (see for details the workflow in Appendix B, Fig. B.1). Our results are illustrated in Fig. 8. With this study we provide a rheological model that highlights the main mechanisms generating: 1) the earthquake distribution in the middle-lower crust, 2) the marked heat flow anomaly in the area SW of the GP.

Rheological models, obtained by using geotherms III and IV, which reproduce the observed surface heat flow, are able to explain brittle deformation and seismicity not only in the domain SW of the GP but also in the NE (Figs. 5 case D, 6 case F) and show some differences among them. It appears that the main parameters affecting the rheological behavior of the crust are the water presence (k_i and λ) and the temperature at the base of the crust T_b. The petrological composition and layer thickness variations affect the thickness of the brittle layer in the lower crust, improving the match with the observed deep seismicity (Figs. 5 case D, 6 case F) .

5.1. Rheology of the GP: implications for seismicity and surface heat flow

As pointed out above the new seismic data acquired by the GSN (Fig. 1A) show that the seismicity of the GP can be subdivided into two main clusters. A first cluster is located in the area SW of the GP and is characterized by a seismicity involving the whole crust down to a depth of 20 km (Miccolis et al., 2021) and surface heat flow $q_0 \approx 100$ mW m^{-2} (Della Vedova et al., 2001). A second cluster involves the whole GP, and is characterized by deep seismicity in the middle-lower crust (Miccolis et al., 2021) and surface heat flow $q_0 \approx 40$ mW m^{-2} (Della Vedova et al., 2001) with foci distributed along a layer gently dipping NE, at depth between 20 and 30 km (Miccolis et al.,

2021).

Cases A and B do not match with the observed surface heat flow and do not produce the expected brittle layer in the lower crust NE of the GP (Figs. 3, 7). Nevertheless, these cases are useful to better understand the role of the model parameters. In case A, brittle behavior is confined within the sedimentary cover only, at depth shallower than 7-8 km. Case B shows that, in presence of rock fracturing, a decrease in cohesion factor S triggers an expansion of the brittle field down to upper crustal depths and in the middle and lower crust a ductile behavior is retained even for fractured condition $S = S_f$, which is incompatible with the deep seismic activity in the GP.

A comparison between the calculated surface heat flow and the values reported in Della Vedova et al. (2001) is shown in Fig. 7. For the cases A and B $q_0(x) = 33$ mW m^{-2}. This value is comparable with heat flow data in the GP, but values in the region SW of the GP are much higher. The high surface heat flow measured in this area could be possibly explained by 1) a heat source at depth, such as melts injected in the crust, and 2) a water circulation system transporting heat at a shallower depth and increasing thermal conductivity in a water-rock phase system. Although the presence of magmatic bodies has been detected both buried (e.g. Loddo et al., 1996) and outcropping in Apulia (e.g. De Fino et al., 1981; Lustrino and Wilson, 2007, and reference therein), there is no recorded magmatic activity younger than 58 Ma in the region. In addition, the presence of buried hot magmatic bodies would increase temperature and favour ductile behavior in host rocks. Therefore, the presence of a shallow water circulation system appears to be a more suitable explanation for both the seismic activity and the high

heat flow near the Candelaro and Apricena faults. This result is further supported by magnetotelluric surveys (Tripaldi, 2020), highlighting the presence of low-resistivity intervals and marked resistivity jumps related to fractured, permeable layers where fluid flow is favoured.

A pivotal role of the interaction between fluids and temperature is shown in cases C-G, where the middle/lower crust is in wet conditions and therefore $S = S_f$, $k = k_w$ and $\lambda = \lambda_w$. In case C, the lower crust shows brittle behavior in the extensional zone ($x < x_{t2}$), with a ductile behavior almost entirely in the compressional zone. However, the seismically active region in the lower crust has a thickness of around 20 km, presumably overlapping the lower and middle crust. In simulations where the upper, middle and lower crust have approximately the same thickness, a granodiorite middle crust composition strongly favors brittle behavior in an extensional zone ($x > x_{t2}$) and when temperature $T_b = 450°C$ (geotherm III, case D). A brittle rheology may also occur in a compressional zone when the middle crust is injected with mafic material (case F) or if the lower crust is particularly thick (case D). It should be noted that the presence of gabbroic rocks in the basement investigated in case F is consistent with the gravimetric anomaly observed both regionally and locally (Loddo et al., 1996; Tassis et al., 2013). It is also important to note that brittle behavior is not predicted when the middle crust is composed of metamorphic rocks derived from sedimentary protholiths, even when injected by mafic rocks (case G). Therefore, it appears that the middle crust has a granodiorite composition and that mafic intrusions could be widespread in the crystalline basement at least at a middle crustal depth (case F).

Our model predicts that brittle deformation is dominant in the sedimentary cover and can further expand down to upper crustal depths in presence of rock faulting. This shows that cataclastic and faulting mechanisms can represent key factors controlling the distribution of earthquakes at shallow depths in both wet and dry conditions. Differently, the middle and lower crust retain a ductile rheology even where the cohesion factor is low ($S = S_f$). The lower crustal composition is dominated by granulite facies metamorphic rocks, which are nominally dry for a wide range of heat flow and heat production conditions (e.g. Jamtveit et al., 2018). Under such conditions, the rheological behavior will be controlled by the strength of the dry mineral assemblage composing the lower crustal rocks, which can exceed 1 GPa (Ranalli and Murphy, 1987). Earthquakes in the lower crust are thus favored by mechanisms capable to significantly decrease the stress threshold for brittle behavior in granulite facies rocks. Our results suggest that an increase in pore fluid pressure λ may constitute a suitable mechanism for rock weakening and subsequent rheology switch from ductile to brittle in the lower crust. The presence of fluids in the lower crust has been well documented in a number of seismic, magnetotelluric and electric studies (e.g. Simpson, 1999, and references therein) and is a trigger for an increase in deformation (e.g. Iio et al., 2002) and seismicity in many different areas (e.g. Deichmann, 1992). This is favored in geodynamic conditions where short-lived, pulsating weakening mechanisms occur (e.g. Noda et al., 2009) and lead to rapid pore fluid pressure variations (Chen and Nur, 1992, and references therein). At the same time, earthquakes in the CF area are less frequent and less energetic than earthquakes occurring in the lower crust of the GP. Therefore, we are

inclined to rule out stress transfer from the CF to the lower crust as main trigger for deeper seismic activity in the GP, although its contribution cannot be excluded. Further studies are evidently needed to better assess the stress transfer role in GP earthquake generation.

In presence of shallow fluid, seismic activity should be not confined only to the lower crust, but it should be more evenly distributed across the crust as it happens in the CF. In contrast, in the GP shallow seismic activity does not occur and, therefore another fluid source is necessary to generate the observed seismicity.

5.2. Origin of fluids and dipping of the lower crust seismogenic layer

The rheological behavior of the GP crystalline basement largely depends on the presence of fluids at depth. However, a fluid source beneath the promontory has not been unambiguously identified. The GP magmatic phase during Palaeogene times was not only restricted to the small dykes today exposed in Punta delle Pietre Nere. It is part of a much more extended magmatic phase, affecting broad sectors in the Adriatic domain (Improta et al., 2014, and references therein) and surrounding regions referred as CiMACI province. The source of this anorogenic magmatic activity is still a matter of debate, but there is a general consensus on mantle plume components characterizing these rocks (e.g. Lustrino and Wilson, 2007). The mantle plumes which may have contributed to the CiMACI province magmatism are often characterized by modest dimensions and low potential temperature, and are therefore difficult to detect (e.g. Kuritani et al., 2017; Koptev et al., 2021). Given the magmatic history of the GP, we suggest that small, local mantle diapiric upwellings or hydrous plumes (e.g. Kuritani et al., 2017; 2019)

could provide volatiles in the lower crust and determine the seismicity that characterizes the area.

Hypocenters beneath the GP show a distribution along a low-angle NE-dipping interval. The orientation of this layer is coherent with regional thrust structures affecting Gargano at shallower depth, generated during middle to upper Miocene NE-SW contractional deformation (Bertotti et al., 1999). Previous studies suggest that aqueous fluids in the continental crust can percolate by porous flow or surface energy-driven infiltration (Watson and Brenan, 1987). These mechanisms are further enhanced along shear zones, where subgrain rotation recrystallization during mylonite formation gives rise to creep cavities (Gilgannon et al., 2020). Therefore, the earthquake hypocenters distribution seems to suggest the presence of a pre-existing deep structure, reactivated by present-day tectonics and where fluids can concentrate due to high relative porosity (Fig. 8). At present day, such structures have not been detected in the Apulian lower crust, although low-angle shear zones have been observed N of GP in the central Adriatic within the upper crust (Finetti and Del Ben, 2005). Therefore, further studies are evidently needed to resolve open questions on the tectonic setting of the Apulian basement and to better comprehend how interactions between fluids presence and tectonics can affect the seismic activity in the GP.

6. Conclusions

Our findings suggest that the prime conditions for seismicity in the lower crust are: presence of wet fractures, low temperatures and appropriate lithological composition. Shallow seismicity SW of the GP in a region where

faulting occurs (CF structure) can probably supply water toward the NE in deeper layers and in particular to the lower crust where seismicity is observed.

The SW shallow seismicity and the NE deeper seismicity could occur along interconnected fractures. However, due to the significant depth where fluid presence occurs and the lack of shallow seismicity in the GP, it is likely that the fluid source is located beneath the crust. Taking into account the history of magmatism that characterizes the GP during Paleocene, we hypothesize that fluid sources are located in the mantle and may persist up to the present day. This requires further investigation by studies aimed to resolve the state of the mantle beneath the GP and the Apulian foreland. This can also lead to better insights into rheological characteristics of the lower crust in other areas, especially in the CiMACI province.

The links between stress release, rock deformation and seismic activity are still poorly investigated in the lower crust. Due to the operation of the GSN that records a continuous low energy seismicity, the GP constitutes a fairly unique opportunity for the interpretation of the mechanisms leading to earthquake nucleation in the lower crust. Therefore, further study of the GP can provide valuable keys for interpretation of rheological patterns and seismic activity in other areas, especially where seismicity is triggered by fluid presence and fluid sources are not well identified.

Acknowledgement

This study was supported by Project PRIN n. 201743P29 FLUIDS (Detection and tracking of crustal fluid by multi-parametric methodologies and technologies). We are grateful to Prof. A. Caggianelli for stimulating discus-

589 sions on the composition of the Apulian crystalline basement. We thank S.
590 Miccolis for the realisation of Fig. 1. We thank an anonymous reviewer for
591 a rigorous review and very constructive comments.

References

Aldersons, F., Ben-Avraham, Z., Hofstetter, A., Kissling, E., Al-Yazjeen, T., 2003. Lower-crustal strength under the Dead Sea basin from local earthquake data and rheological modeling. Earth and Planetary Science Letters 214, 129–142. doi:10.1016/S0012-821X(03)00381-9.

Aliaj, S., 2006. The Albanian Orogen: Convergence Zone between Eurasia and the Adria Microplate, in: Pinter, N., Gyula, G., Weber, J., Stein, S., Medak, D. (Eds.), The Adria Microplate: GPS Geodesy, Tectonics and Hazards, Springer Netherlands, Dordrecht. pp. 133–149.

Amato, A., Bianchi, I., Agostinetti, N., 2014. Apulian crust: Top to bottom. Journal of Geodynamics 82, 125–137.

Argnani, A., Rovere, M., Bonazzi, C., 2009. Tectonics of the Mattinata fault, offshore south Gargano (southern Adriatic Sea, Italy): Implications for active deformation and seismotectonics in the foreland of the Southern Apennines. Bulletin of the Geological Society of America 121, 1421–1440.

Audin, L., Avouac, J.P., Flouzat, M., Plantet, J.L., 2002. Fluid-driven seismicity in a stable tectonic context: The Remiremont fault zone, Vosges, France. Geophysical Research Letters 29. doi:10.1029/2001GL012988.

Babbucci, D., Tamburelli, C., Viti, M., Mantovani, E., Albarello, D., D'Onza, F., Cenni, N., Mugnaioli, E., 2004. Relative motion of the Adriatic with respect to the confining plates: Seismological and geodetic constraints. Geophysical Journal International 159, 765–775.

614 Battaglia, M., Murray, M., Serpelloni, E., Burgmann, R., 2004. The Adri-
615 atic region: An independent microplate within the Africa-Eurasia collision
616 zone. Geophysical Research Letters 31, L09605 1–4.

617 Benson, P., Austria, D., Gehne, S., Butcher, E., Harnett, C., Fazio, M.,
618 Rowley, P., Tomas, R., 2020. Laboratory simulations of fluid-induced seis-
619 micity, hydraulic fracture, and fluid flow. Geomechanics for Energy and
620 the Environment 24. doi:10.1016/j.gete.2019.100169.

621 Bertotti, G., Casolari, E., Picotti, V., 1999. The Gargano Promontory: A
622 Neogene contractional belt within the Adriatic plate. Terra Nova 11, 168–
623 173.

624 Bigazzi, G., Laurenzi, M., Principe, C., D., B., 1996. New geochronological
625 data on igneous rocks and evaporites of the Pietre Nere Point (Gargano
626 peninsula, southern Italy). Boll. Soc. Geol. Ital. 115, 439–448.

627 Brankman, C., Aydin, A., 2004. Uplift and contractional deformation along
628 a segmented strike-slip fault system: The Gargano Promontory, southern
629 Italy. Journal of Structural Geology 26, 807–824.

630 Burov, E.B., 2011. Rheology and strength of the lithosphere. Marine and
631 Petroleum Geology 28, 1402–1443. doi:10.1016/j.marpetgeo.2011.05.008.

632 Campbell, L., Menegon, L., Fagereng, Å., Pennacchioni, G., 2020. Earth-
633 quake nucleation in the lower crust by local stress amplification. Nature
634 Communications 11.

635 Carmichael, R., 2017. Handbook of Physical Properties of Rocks (1982):
636 Volume II. CRC Press Revivals, CRC Press.

637 Chen, Q., Nur, A., 1992. Pore fluid pressure effects in anisotropic rocks:
638 Mechanisms of induced seismicity and weak faults. Pure and Applied
639 Geophysics PAGEOPH 139, 463–479. doi:10.1007/BF00879947.

640 Chen, W.P., Molnar, P., 1983. Focal depths of intracontinental and intraplate
641 earthquakes and their implications for the thermal and mechanical prop-
642 erties of the lithosphere. Journal of Geophysical Research: Solid Earth 88,
643 4183–4214.

644 Clauser, C., Huenges, E., 1995. Thermal Conductivity of Rocks and Minerals.
645 American Geophysical Union (AGU). pp. 105–126.

646 Cloetingh, S., Burov, E., 1996. Thermomechanical structure of European
647 continental lithosphere: Constraints from rheological profiles and EET
648 estimates. Geophysical Journal International 124, 695–723.

649 D'Agostino, N., Avallone, A., Cheloni, D., D'Anastasio, E., Mantenuto, S.,
650 Selvaggi, G., 2008. Active tectonics of the Adriatic region from GPS and
651 earthquake slip vectors. Journal of Geophysical Research: Solid Earth 113.

652 De Fino, M., La Volpe, L., Piccarreta, G., 1981. Geochemistry and petro-
653 genesis of the Paleocene platform magmatism at Punta delle Pietre Nere
654 (southeastern Italy). Neues Jahrbuch fur Mineralogie, Abhandlungen 142,
655 161–177.

656 Deichmann, N., 1992. Structural and rheological implications of lower-crustal
657 earthquakes below northern Switzerland. Physics of the Earth and Plane-
658 tary Interiors 69, 270–280.

659 Del Gaudio, V., Pierri, P., Frepoli, A., Calcagnile, G., Venisti, N., Cimini,
660 G., 2007. A critical revision of the seismicity of Northern Apulia (Adri-
661 atic microplate - Southern Italy) and implicationsfor the identification of
662 seismogenic structures. Tectonophysics 436, 9–35.

663 Della Vedova, B., Bellani, S., Pellis, G., Squarci, P., 2001. Deep temperatures
664 and surface heat flow distribution. Springer Netherlands, Dordrecht. pp.
665 65–76.

666 Déverchère, J., Petit, C., Gileva, N., Radziminovitch, N., Melnikova, V.,
667 San'Kov, V., 2001. Depth distribution of earthquakes in the Baikal rift
668 system and its implications for the rheology of the lithosphere. Geophysical
669 Journal International 146, 714–730.

670 Dragoni, M., Doglioni, C., Mongelli, F., Zito, G., 1996. Evaluation of stresses
671 in two geodynamically different areas: Stable foreland and extensional
672 backarc. Pure and Applied Geophysics 146, 319–341.

673 El Hariri, M., Abercrombie, R., Rowe, C., do Nascimento, A., 2010. The role
674 of fluids in triggering earthquakes: Observations from reservoir induced
675 seismicity in Brazil. Geophysical Journal International 181, 1566–1574.
676 doi:10.1111/j.1365-246X.2010.04554.x.

677 Fagereng, Å., Biggs, J., 2019. New perspectives on 'geological strain rates'
678 calculated from both naturally deformed and actively deforming rocks.
679 Journal of Structural Geology 125, 100–110. doi:10.1016/j.jsg.2018.10.004.

680 Filippucci, M., Del Pezzo, E., de Lorenzo, S., Tallarico, A., 2019a. 2D kernel-

based imaging of coda-Q space variations in the Gargano Promontory (Southern Italy). Physics of the Earth and Planetary Interiors 297.

Filippucci, M., Lucente, S., Del Pezzo, E., de Lorenzo, S., Prosser, G., Tallarico, A., 2021a. 3d-kernel based imaging of an improved estimation of (Qc) in the northern apulia (southern italy). Applied Sciences (Switzerland) 11. doi:10.3390/app11167512.

Filippucci, M., Miccolis, S., Castagnozzi, A., Cecere, G., de Lorenzo, S., Donvito, G., Falco, L., Michele, M., Nicotri, S., Romeo, A., Selvaggi, G., Tallarico, A., 2021b. Seismicity of the Gargano promontory (Southern Italy) after 7 years of local seismic network operation: Data release of waveforms from 2013 to 2018. Data in Brief 35.

Filippucci, M., Pierri, P., de Lorenzo, S., Tallarico, A., 2020. The Stress Field in the Northern Apulia (Southern Italy), as Deduced from Microearthquake Focal Mechanisms: New Insight from Local Seismic Monitoring. Lecture Notes in Computer Science (including subseries Lecture Notes in Artificial Intelligence and Lecture Notes in Bioinformatics) 12255 LNCS, 914–927.

Filippucci, M., Tallarico, A., Dragoni, M., de Lorenzo, S., 2019b. Relationship Between Depth of Seismicity and Heat Flow: The Case of the Gargano Area (Italy). Pure and Applied Geophysics 176, 2383–2394.

Finetti, I., Del Ben, A., 2005. Crustal Tectono-Stratigraphic Setting of the Adriatic Sea from New CROP Seismic Data. Elsevier, Amsterdam. volume 1. pp. 519–548.

Gardonio, B., Jolivet, R., Calais, E., Leclère, H., 2018. The April 2017 Mw6.5 Botswana Earthquake: An Intraplate Event Triggered by Deep Fluids. Geophysical Research Letters 45, 8886–8896.

Gerya, T., 2009. Numerical solution of the heat conservation equation. Cambridge University Press. pp. 133–148.

Gilgannon, J., Poulet, T., Berger, A., Barnhoorn, A., Herwegh, M., 2020. Dynamic Recrystallization Can Produce Porosity in Shear Zones. Geophysical Research Letters 47.

Girard, J., Chen, J., Raterron, P., Holyoke, C., 2013. Hydrolytic weakening of olivine at mantle pressure: Evidence of [100](010) slip system softening from single-crystal deformation experiments. Physics of the Earth and Planetary Interiors 216, 12–20. doi:10.1016/j.pepi.2012.10.009.

Gruber, B., Chacko, T., Pearson, D., Currie, C., Menzies, A., 2021. Heat production and moho temperatures in cratonic crust: evidence from lower crustal xenoliths from the slave craton. Lithos 380-381. doi:10.1016/j.lithos.2020.105889.

Hecht, F., 2012. New development in freefem+. Journal of Numerical Mathematics 20, 251–265.

Heidbach, O., Rajabi, M., Reiter, K., Ziegler, M.O., 2019. World Stress Map. Springer International Publishing, Cham. pp. 1–8.

Iio, Y., Sagiya, T., Kobayashi, Y., Shiozaki, I., 2002. Water-weakened lower crust and its role in the concentrated deformation in the Japanese Islands. Earth and Planetary Science Letters 203, 245–253.

727 Improta, L., De Gori, P., Chiarabba, C., 2014. New insights into crustal
728 structure, Cenozoic magmatism, CO_2 degassing, and seismogenesis in the
729 southern Apennines and Irpinia region from local earthquake tomography.
730 Journal of Geophysical Research: Solid Earth 119, 8283–8311.

731 Jamtveit, B., Ben-Zion, Y., Renard, F., Austrheim, H., 2018. Earthquake-
732 induced transformation of the lower crust. Nature 556, 487–491.

733 Jamtveit, B., Petley-Ragan, A., Incel, S., Dunkel, K., Aupart, C., Aus-
734 trheim, H., Corfu, F., Menegon, L., Renard, F., 2019. The Effects of
735 Earthquakes and Fluids on the Metamorphism of the Lower Continen-
736 tal Crust. Journal of Geophysical Research: Solid Earth 124, 7725–7755.
737 doi:10.1029/2018JB016461.

738 Ji, S., Zhao, P., Xia, B., 2003. Flow laws of multiphase materials and rocks
739 from end-member flow laws. Tectonophysics 370, 129–145.

740 Koptev, A., Cloetingh, S., Ehlers, T., 2021. Longevity of small-scale (baby)
741 plumes and their role in lithospheric break-up. Geophys. J. Int.227, 439-
742 471. .

743 Kuritani, T., Sakuyama, T., Kamada, N., Yokoyama, T., Nakagawa, M.,
744 2017. Fluid-fluxed melting of mantle versus decompression melting of hy-
745 drous mantle plume as the cause of intraplate magmatism over a stagnant
746 slab: Implications from Fukue Volcano Group, SW Japan. Lithos 282-283,
747 98–110.

748 Lavecchia, A., Clark, S., Beekman, F., Cloetingh, S., Burov, E., 2016. Ther-

749 mal perturbation, mineral assemblages, and rheology variations induced
750 by dyke emplacement in the crust. Tectonics 35, 1137–1152.

751 Lenkey, L., P, D., Horvath, F., Cloetingh, S., 2002. Geothermics of the
752 Pannonian basin and its bearing on the neotectonics. Stephan Mueller
753 Special Publication Series 3.

754 Loddo, M., Quarto, R., Schiavone, D., 1996. Integrated geophysical sur-
755 vey for the geological structural and hydrogeothermal study of the North-
756 western Gargano promontory (Southern Italy). Annali di Geofisica 39,
757 201–219.

758 Lustrino, M., Wilson, M., 2007. The circum-Mediterranean anorogenic Ceno-
759 zoic igneous province. Earth-Science Reviews 81, 1–65.

760 Maggi, A., Jackson, J., McKenzie, D., Priestley, K., 2000. Earthquake fo-
761 cal depths, effective elastic thickness, and the strength of the continental
762 lithosphere. Geology 28, 495–498.

763 Mazzeo, F., Arienzo, I., Aulinas, M., Casalini, M., Di Renzo, V., D'Antonio,
764 M., 2018. Mineralogical, geochemical and isotopic characteristics of alka-
765 line mafic igneous rocks from Punta delle Pietre Nere (Gargano, Southern
766 Italy). Lithos 308-309, 316–328.

767 Meissner, R., Kern, H., 2008. Earthquakes and strength in the laminated
768 lower crust -Can they be explained by the "corset model"? Tectonophysics
769 448, 49–59. doi:10.1016/j.tecto.2007.11.034.

770 Menegon, L., Fusseis, F., Stünitz, H., Xiao, X., 2015. Creep cavitation bands

771 control porosity and fluid flow in lower crustal shear zones. Geology 43,
772 227–230. doi:10.1130/G36307.1.

773 Miccolis, S., Filippucci, M., de Lorenzo, S., Frepoli, A., Pierri, P., 2021. Seis-
774 mogenic structures orientation and stress field of the Gargano Promontory
775 (southern Italy) from microseismicity analysis. Frontiers in Earth Science.

776 Morsili, M., 2016. Sintesi delle conoscenze geologiche e stratigra che del
777 Promontorio del Gargano. Geol. Terr. 3, 15–30.

778 Neely, J.S., Stein, S., 2021. Why do continental normal fault earth-
779 quakes have smaller maximum magnitudes? Tectonophysics 809, 228854.
780 doi:https://doi.org/10.1016/j.tecto.2021.228854.

781 Noda, H., Dunham, E., Rice, J., 2009. Earthquake ruptures with
782 thermal weakening and the operation of major faults at low over-
783 all stress levels. Journal of Geophysical Research: Solid Earth 114.
784 doi:10.1029/2008JB006143.

785 Oldow, J., Ferranti, L., Lewis, D., Campbell, J., D'Argenio, B., Catalano,
786 R., Pappone, G., Carmignani, L., Conti, P., Aiken, C., 2002. Active frag-
787 mentation of Adria, the north African promontory, central Mediterranean
788 orogen. Geology 30, 779–782.

789 Pasquale, V., Cabella, C., Verdoya, M., 1990. Deep temperatures and litho-
790 spheric thickness along the European Geotraverse. Tectonophysics 176,
791 1–11. doi:10.1016/0040-1951(90)90255-7.

792 Philpotts, A., Ague, J., 2009. Principles of Igneous and Metamorphic Petrol-
793 ogy. 2 ed., Cambridge University Press. doi:10.1017/CBO9780511813429.

794 Ranalli, G., 1995. Rheology of the Earth. Chapman and Hall, London, U.K.

795 Rovida, A., Locati, M., Camassi, R., Lolli, B., Gasperini, P., 2019. Catalogo
796 Parametrico dei Terremoti Italiani (CPTI15), versione 2.0.

797 Salamon, A., Hofstetter, A., Garfunkel, Z., Ron, H., 2003. Seismotectonics
798 of the Sinai subplate - The eastern Mediterranean region. Geophysical
799 Journal International 155, 149–173.

800 Schenk, V., 1981. Synchronous uplift of the lower crust of the Ivrea Zone
801 and of Southern Calabria and its possible consequences for the Hercynian
802 orogeny in Southern Europe. Earth and Planetary Science Letters 56,
803 305–320.

804 Schutt, D., Lowry, A., Buehler, J., 2018. Moho temperature and mobil-
805 ity of lower crust in the western United States. Geology 46, 219–222.
806 doi:10.1130/G39507.1.

807 Shudofsky, G., Cloetingh, S., Stein, S., Wortel, R., 1987. Unusually deep
808 earthquakes in East Africa: Constraints on the thermo-mechanical struc-
809 ture of a continental rift system. Geophysical Research Letters 14, 741–744.

810 Simpson, F., 1999. Stress and seismicity in the lower continental crust: A
811 challenge to simple ductility and implications for electrical conductivity
812 mechanisms. Surveys in Geophysics 20, 201–227.

813 Smith, S., Faulkner, D., 2010. Laboratory measurements of the frictional
814 properties of the Zuccale low-angle normal fault, Elba Island, Italy. Journal
815 of Geophysical Research: Solid Earth 115.

816 Stein, S., Sella, G.F., 2006. Pleistocene change from convergence to exten-
817 sion in the Apennines as a consequence of Adria microplate motion, in:
818 Pinter, N., Gyula, G., Weber, J., Stein, S., Medak, D. (Eds.), The Adria
819 Microplate: GPS Geodesy, Tectonics and Hazards, Springer Netherlands,
820 Dordrecht. pp. 21–34.

821 Tassis, G., Grigoriadis, V., Tziavos, I., Tsokas, G., Papazachos, C., Vasiljević,
822 I., 2013. A new Bouguer gravity anomaly field for the Adriatic Sea and
823 its application for the study of the crustal and upper mantle structure.
824 Journal of Geodynamics 66, 38–52.

825 Tripaldi, S., 2020. Electrical signatures of a permeable zone in carbonates
826 hosting local geothermal manifestations: Insights for the deep fluid flow in
827 the Gargano area (South-eastern Italy). Bollettino di Geofisica Teorica ed
828 Applicata 61, 219–232.

829 Tullis, J., Yund, R., 1989. Hydrolytic weakening of quartz aggregates: The
830 effects of water and pressure on recovery. Geophysical Research Letters
831 16, 1343–1346. doi:10.1029/GL016i011p01343.

832 Van Dinther, Y., Gerya, T., Dalguer, L., Mai, P., Morra, G., Giardini, D.,
833 2013. The seismic cycle at subduction thrusts: Insights from seismo-
834 thermo- mechanical models. Journal of Geophysical Research: Solid Earth
835 118, 6183–6202.

836 Wang, Z., Shi, F., Zhang, J., 2020. Effects of Water on the Rheology of
837 Dominant Minerals and Rocks in the Continental Lower Crust: A Review.
838 Journal of Earth Science 31, 1170–1182. doi:10.1007/s12583-020-1307-9.

839 Watson, E., Brenan, J., 1987. Fluids in the lithosphere, 1. Experimentally-
840 determined wetting characteristics of CO2 H2O fluids and their implica-
841 tions for fluid transport, host-rock physical properties, and fluid inclusion
842 formation. Earth and Planetary Science Letters 85, 497–515.

843 Winter, T., Tapponnier, P., 1991. Post-Jurassic-pre-Miocene major exten-
844 sion in central Italy; microtectonic evidence [Extension majeure post-
845 Jurassique et ante-Miocene dans le centre de l'Italie: donnees microtec-
846 toniques]. Bulletin - Societe Geologique de France 162, 1095–1108.

847 Yin, Z.M., Ranalli, G., 1992. Critical stress difference, fault orientation and
848 slip direction in anisotropic rocks under non-Andersonian stress systems.
849 Journal of Structural Geology 14, 237–244.

Tables

A

Parameter	Symbol	Value	U.m.
Surface temperature ($z = 0$)	T_0	20	°C
Base temperature ($z = z_6$) (Geotherm I and II)	T_b	500	°C
Base temperature ($z = z_6$) (Geotherm III and IV)	T_b	450	°C
Surface Radiogenic heat production ($z = 0$)	H_0	2	μW m^{-3}
Acceleration of gravity	g	9.8	m s^{-2}
Characteristic depth	D	12	km
Gas constant	R	8.314	J K^{-1}mol^{-1}
Thermal expansion coefficient††	α	$5 \cdot 10^{-6}$	K^{-1}
Friction coefficient‡‡	κ	0.5	-
Strain rate‡	$\dot{\varepsilon}$	10^{-14}	s^{-1}
Solver minimal residual	ζ	10^{-6}	-
Cohesion factor** (fractured; unfractured)	$S_f; S_u$	10; 75	MPa
Pore fluid factor** (dry; wet)	$\lambda_d; \lambda_w$	0.4; 0.8	-

B

Parameter	Symbol	Layer i						U.m.
		1	2	3	4	5	6	
Layer depth bottom	z_i	2.5*	5.5*	8	16	24	32	km
Layer thickness	th_i	5.5*	3*	2.5	8	8	8	km
Layer depth bottom (case D)	z_i	2.5*	5.5*	8	14	20	32	km
Layer thickness (case D)	th_i	5.5*	3*	2.5	6	6	12	km
Surface density**	ρ_{0i}	2450	2250	2500	2750	2800	2900	kg m^{-3}
Specific heat at c. p.	C_{pi}	800	800	800	1000	1000	1000	J K^{-1} kg^{-1}
Conductivity† (dry)	k_{di}	2.1	2.0	2.5	2.7	2.5	2.4	W K^{-1} m^{-1}

Table 1: Parameters of the model. A) independent on layer, B) dependent on layer. (*Amato et al. (2014); **Carmichael (2017); †Clauser and Huenges (1995); ††Gerya (2009); ‡Ranalli (1995); ‡‡Smith and Faulkner (2010) and references therein).

A

Parameter		Symbol	Cases							U.m.
			A	B	C	D	E	F	G	
Geotherm			I	I	**II**	**III**	**IV**	IV	IV	
Depth bottom of layer 4		z_4	16	16	16	**14**	**16**	16	16	km
Depth bottom of layer 5		z_5	24	24	24	**20**	**24**	24	24	km
Base temperature		T_b	500	500	500	**450**	450	450	450	°C
Cohesion factor	Unfractured	S_u	75	75	75	75	75	75	75	MPa
	Fractured	S_f	-	**10**	10	10	10	10	10	
Pore fluid factor	Dry	λ_d	0.4	0.4	0.4	0.4	0.4	0.4	0.4	-
	Wet	λ_w	-	-	**0.8**	0.8	0.8	0.8	0.8	
Presence of mafic rocks			No	No	No	No	No	**Yes**	Yes	
Sedimentary protholith in layer 5			No	No	No	No	No	No	**Yes**	

B

Layer	Composition	A_i	n_i	Q_i
i	% vol	$\mathrm{MPa^{-n}s^{-1}}$	–	$\mathrm{kJ\ mol^{-1}}$
1	Cc65, Qtz10, Dm25	$2.4 \cdot 10^{-1}$	3.28	182
2	Qtz20, Dm80	$3.3 \cdot 10^{-6}$	3.18	161
3	Cc10, Mc30, Qtz30, Dm10, Ab20	$1.7 \cdot 10^{-6}$	6.23	163
4	Cc5, Mc35, Qtz35, Ab15, Als5, An5	$6.9 \cdot 10^{-8}$	7.15	173
5	Mc15, Qtz30, Ab35, An20	$3.4 \cdot 10^{-6}$	5.00	204
5 (case F)	Mc10, Qtz20, Ab23, An23, Px20, Ol4	$1.2 \cdot 10^{-10}$	4.26	236
5 (case G)	Mc24, Qtz19, Ab21, An9, Px23, Ol4	$2.7 \cdot 10^{-5}$	5.37	212
6	Mc12, Qtz25, Ab25, Als7, Grt14, Px14, Ol3	$2.8 \cdot 10^{-4}$	4.70	269
6 (case F)	Mc8, Qtz17, Ab16, Als5, Grt9, Px29, Ol5	$1.9 \cdot 10^{-3}$	4.10	269

Table 2: A) Parameters adopted for each case. Bold characters indicate variations in parameters with respect to the preceding case. B) Mineral assemblage and resulting rheological parameters for each layer. A_i, n_i and Q_i values relative to single minerals are given in Lavecchia et al. (2016) and references therein. See text for the description of the methodology adopted to calculate A_i, n_i, and Q_i. Cc = calcite, Qtz = quartz, Dm = dolomite, Mc = phyllosilicates, Ab = albite, Als = aluminosilicates, An = anorthite, Px = pyroxene, Ol = olivine, Grt = garnet.

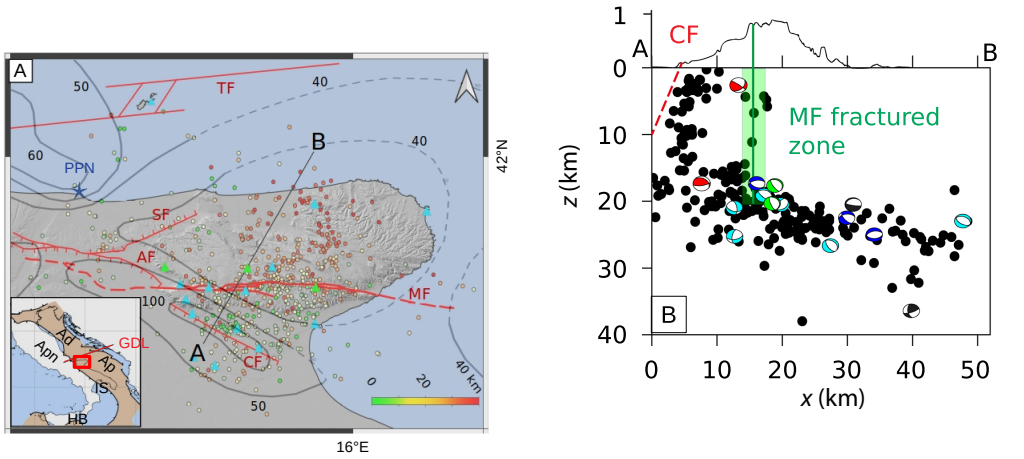

Figure 1: A) Map of the Gargano promontory. The transect shows its location (red square) with respect to the Adria and Apulian microplates (brown area, Ad=Adria microplate, Ap=Apulian microplate, Apn=Apennines, HB=Hyblean block, IS=Ionian Sea) (D'Agostino et al., 2008); the red segment is the Gargano-Dubrovnik lineament (GDL) (after Battaglia et al., 2004). Earthquakes are indicated by small circles colored according to depth (Miccolis et al., 2021). Triangles represent the GSN network seismic stations (IV: blue, OT: green). Grey lines are the isolines of surface heat flow (mW m^{-2}) (Della Vedova et al., 2001). Red lines are the main faults (AF=Apricena Fault; CF=Candelaro Fault; MF=Mattinata Fault; SF=Sannicandro Fault; TF=Tremiti Fault, modified from Miccolis et al. (2021)). Blue star indicates Punta delle Pietre Nere (PPN). The A-B black segment is the trace of the vertical crustal section in panel A and B. B) Vertical cross-section along the A-B section: hypocenters (black circles) and focal mechanisms are projected over the vertical plane (red=normal; green=transcurrent; light blue=transpressive; dark blue=compressive; black=unknown). Red line indicates the CF, green line and green area indicate the MF fractured zone (after Miccolis et al. (2021)).

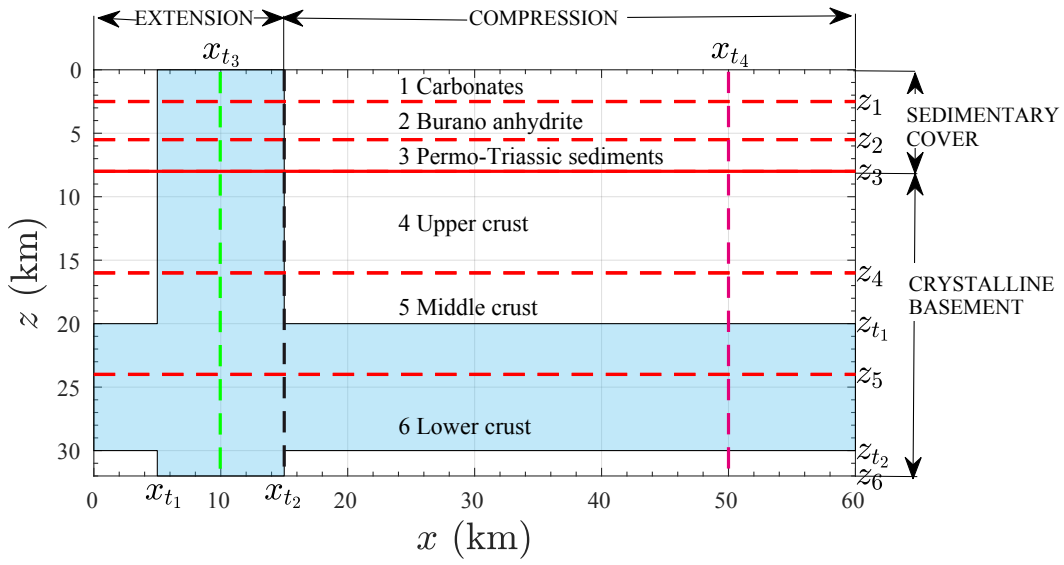

Figure 2: Sketch of the model. Horizontal lines: the dashed red lines indicate the i-th layers boundary ($z = z_i$), the solid red line indicates the boundary between the sedimentary cover and the crystalline basement ($z = z_3$). Vertical lines: the green ($x = x_{t3}$) and magenta ($x = x_{t4}$) dashed lines indicate the two vertical profiles where significant model results are calculated, the black dashed line ($x = x_{t2}$) indicates the boundary between extensional and compressional tectonic regime. The light blue area is affected by the presence of fluids, fracturing or both.

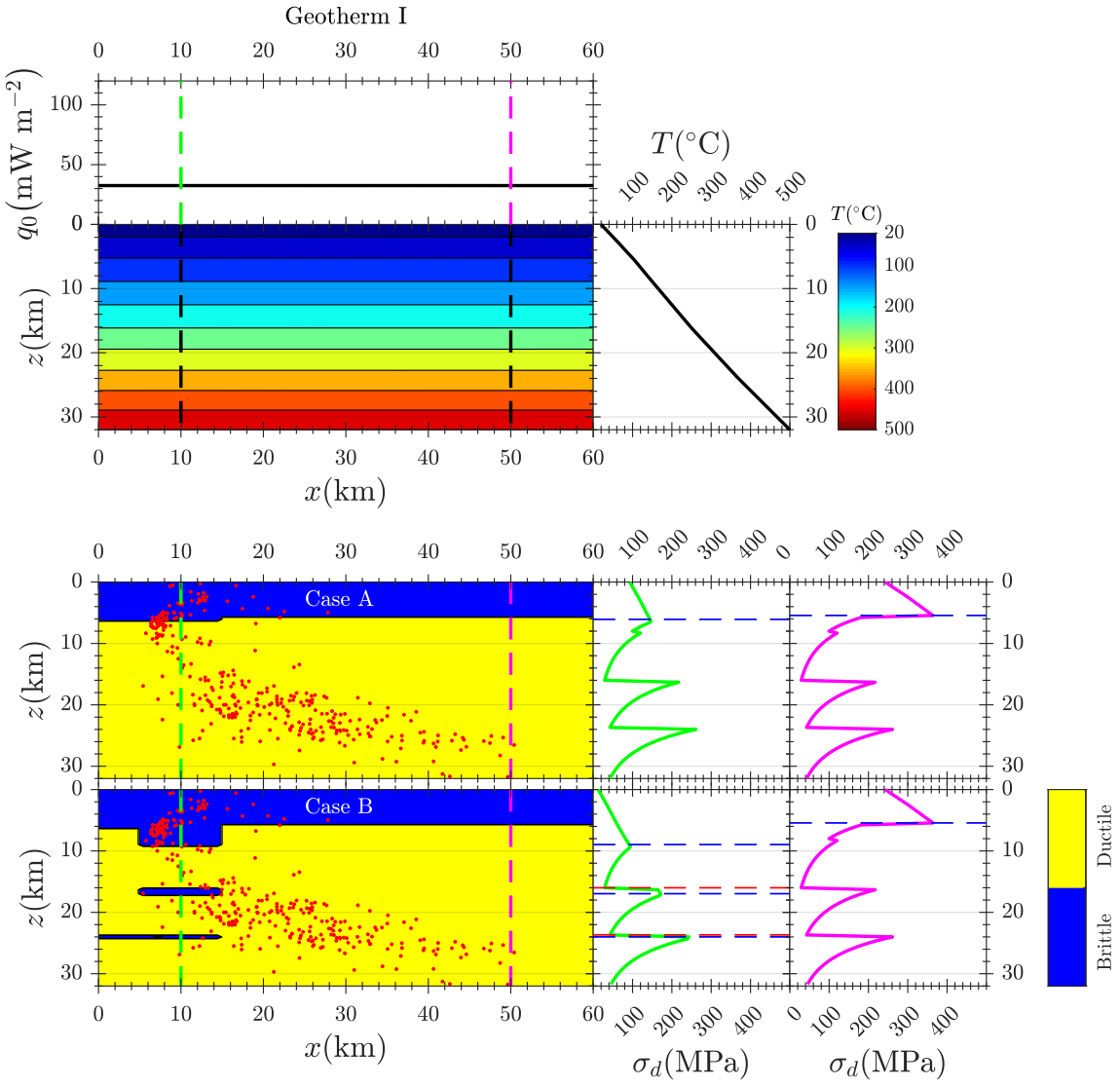

Figure 3: Geotherm I and Cases A and B. Upper panel: 2D Temperature $T(x, z)$, surface heat flow $q_0(x)$, temperature $T(z)$ along the black vertical dashed lines. $T_b = 500\,^{\circ}\mathrm{C}$. Lower panels: rheological structure $Rh(x, z)$, differential stress $\sigma_d(z)$ with colours referring to the vertical dashed lines. Horizontal dashed lines refer to the brittle-to-ductile boundary (color blue) and to the ductile-to-brittle boundary (color red) for increasing depth. Case A: dry unfractured condition, Case B: dry fractured condition in the light blu area of Fig. 2. The parameters adopted to plot the graphs are shown in Tables 1, 2.

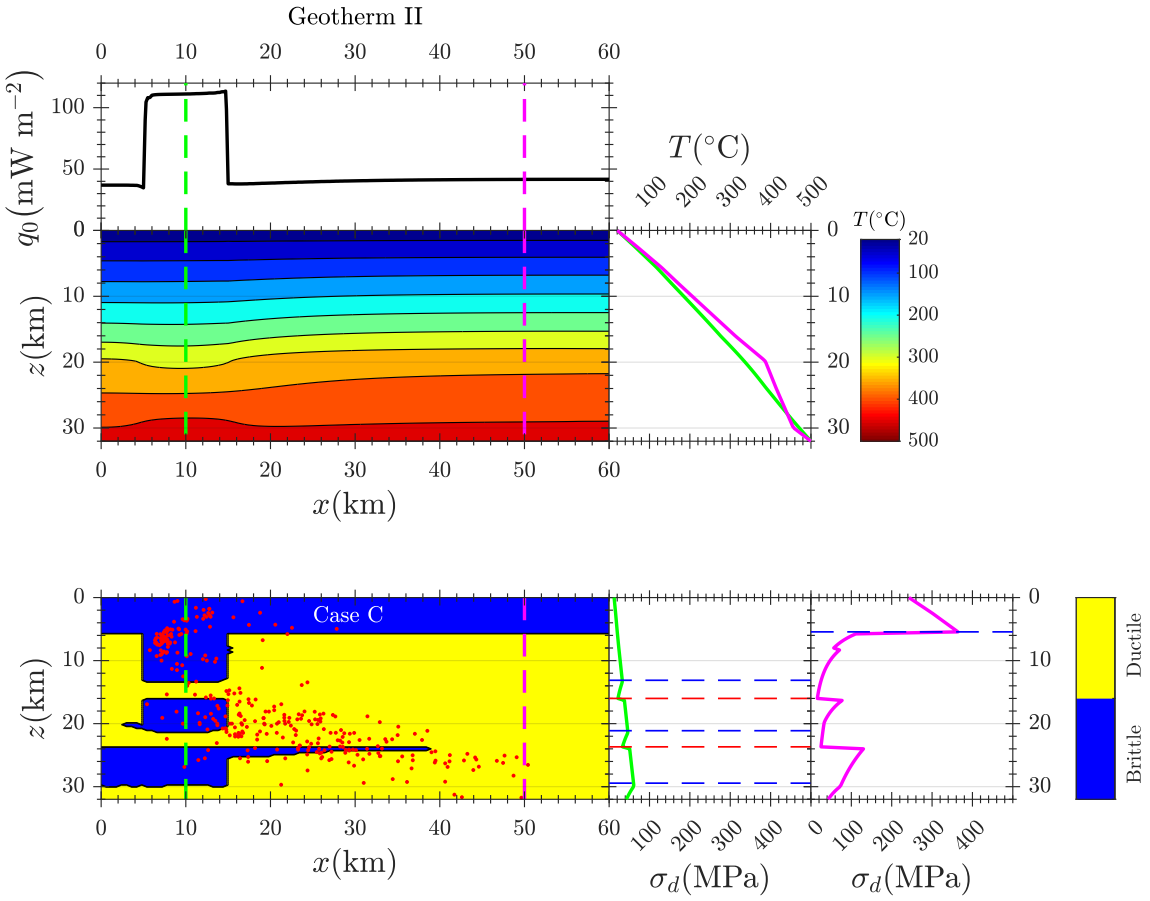

Figure 4: Geotherm II and Case C. Upper panel: 2D Temperature $T(x, z)$, surface heat flow $q_0(x)$, temperature $T(z)$ with colours referring to the vertical dashed lines. T_b = 500 °C . Lower panels: rheological structure $Rh(x, z)$, differential stress $\sigma_d(z)$ with colours referring to the vertical dashed lines. Horizontal dashed lines refer to the brittle-to-ductile boundary (color blue) and to the ductile-to-brittle boundary (color red) for increasing depth. Case C: wet and fractured condition in the light blu area of Fig. 2. The parameters adopted to plot the graphs are shown in Tables 1, 2.

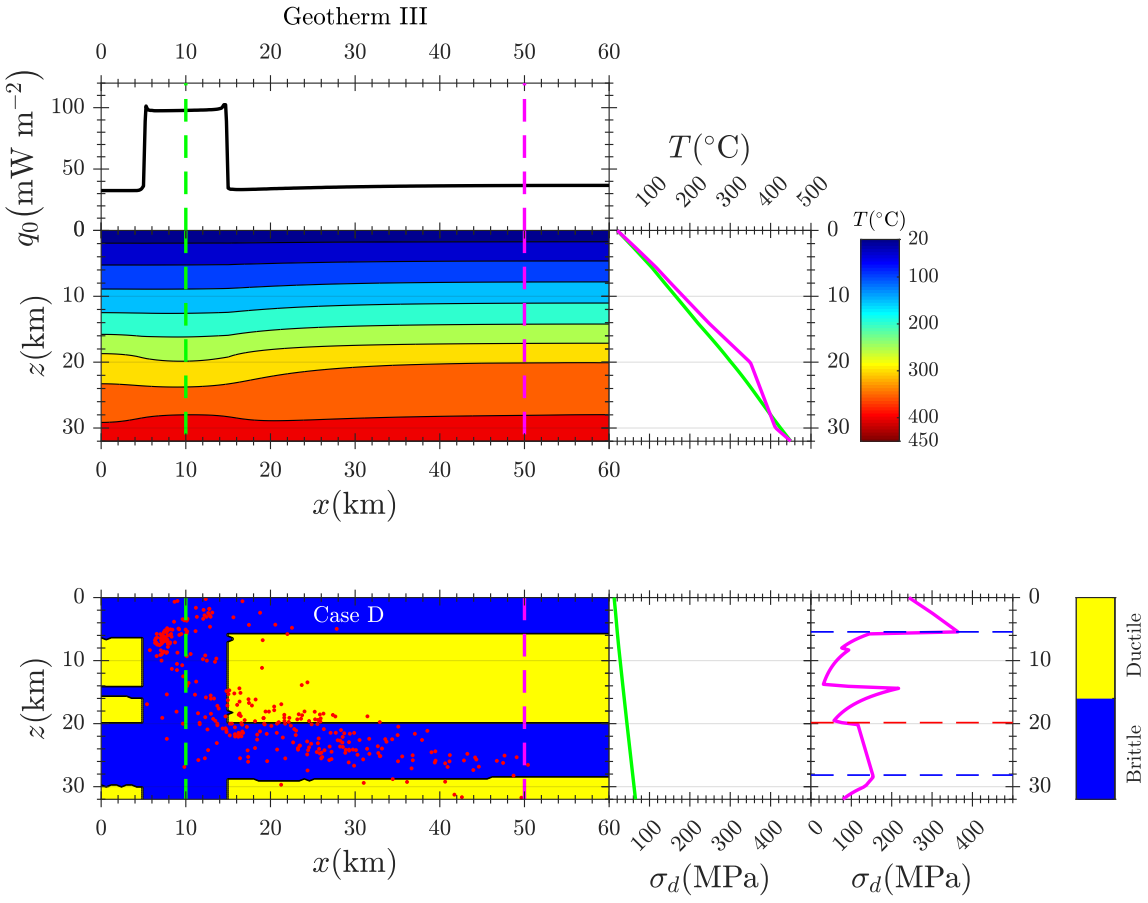

Figure 5: Geotherm III and Case D. Upper panel: 2D Temperature $T(x, z)$, surface heat flow $q_0(x)$, temperature $T(z)$ with colours referring to the vertical dashed lines. T_b = 450 °C . Lower panels: rheological structure $Rh(x, z)$, differential stress $\sigma_d(z)$ with colours referring to the vertical dashed lines. Horizontal dashed lines refer to the brittle-to-ductile boundary (color blue) and to the ductile-to-brittle boundary (color red) for increasing depth. Case D: wet and fractured condition in the light blu area of Fig. 2, lower crust thicker. The parameters adopted to plot the graphs are shown in Tables 1, 2.

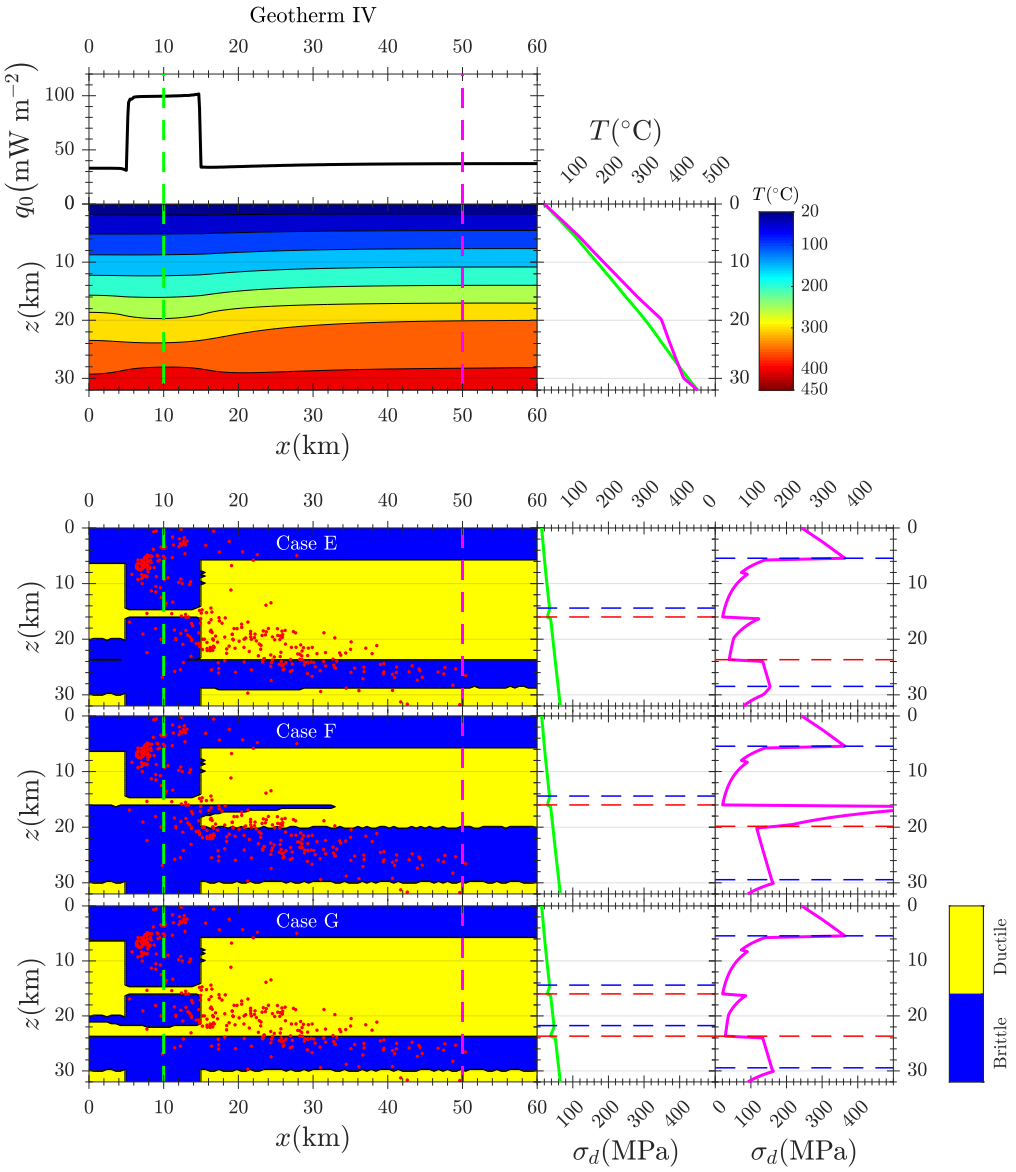

Figure 6: Geotherm IV and Cases E, F, G. Upper panel: 2D Temperature $T(x, z)$, surface heat flow $q_0(x)$, temperature $T(z)$ with colours referring to the vertical dashed lines. $T_b = 450$ °C . Lower panels: rheological structure $Rh(x, z)$, differential stress $\sigma_d(z)$ with colours referring to the vertical dashed lines. Horizontal dashed lines refer to the brittle-to-ductile boundary (color blue) and to the ductile-to-brittle boundary (color red) for increasing depth. For all cases : wet and fractured condition in the light blu area of Fig. 2. Case F: Gabbros. Case G: Gabbros+metasediment. The parameters adopted to plot the graphs are shown in Tables 1, 2.

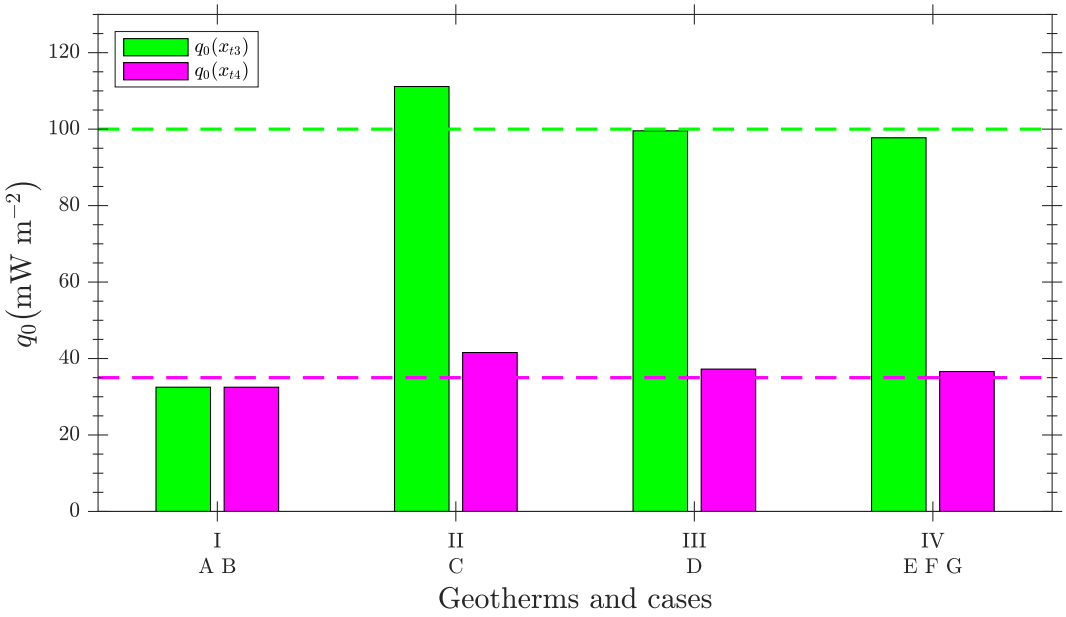

Figure 7: Comparison between surface vertical heat flow $q_0(x_{t3})$ and $q_0(x_{t4})$ calculated by the model (bars) and reported in Della Vedova et al. (2001) (dashed lines). The green and magenta colors refer to the points $x = x_{t3}$ and $x = x_{t4}$ shown in Fig. 2 respectively. Case D represents the best agreement between calculated and measured values of q_0.

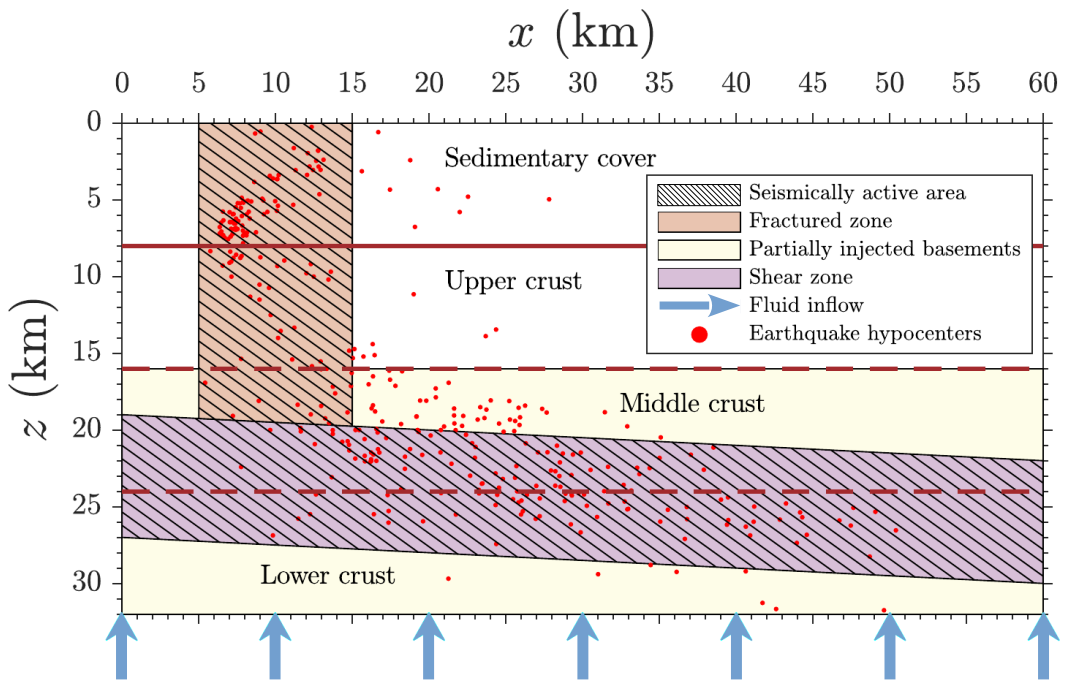

Figure 8: Conceptual framework for the lithology, tectonic structures and role of fluids for crustal seismicity, illustrated by schematic cross-section of the studied area, inferred from our model. Moho is taken at a depth of 32 km. The presence of fractures and faults affects the sedimentary cover and shallow levels of the crystalline basement. The basement is partly composed of mafic rocks. The fractures can represent favorable intervals for fluid circulation. In proximity of the crustal base, a deep fluid source can provide fluids that collect along shear zones, where porosity is greater than in the surrounding rocks. Hatched areas mark the envelope of the depth distribution of seismicity.

Appendix A. Lithologies constituting the crustal layers

In our simulations the rheological behavior of the rocks constituting each layer is calculated on the basis of a polymineralic composition of the GP crust. More in detail, we assume a polyphase composition of each model layer, taking into account the rheological parameters of each mineral and their volume percentage in the rocks. The mineral assemblage and the volume percentage of minerals composing the layers are based on average compositions for the lithologies occurring in the GP (e.g. Philpotts and Ague, 2009) and are illustrated in Table 2.

1. Carbonate rocks (limestone and dolostone), locally interbedded with chert layers, with age ranging between upper Jurassic and Eocene. These rocks are by far the most common lithologies outcropping in the GP. Locally they can be covered by Quaternary sediments, that are discontinuous and with modest thickness and are not incorporated in the simulations.
2. Anhydrite, limestones and dolostones, corresponding to the Anidriti di Burano formation. These rocks have upper Triassic age (Carnian-Rhaetian) and variable thickness.
3. Permo-Triassic clastic continental rocks. In the lowermost part, this formation is constituted by low degree phyllites, with possible presence of intrusive bodies.
4. Upper crust phyllites, micaschists and paragneisses with intercalate metavolcanic rocks and marbles.
5. Carboniferous plutonic rocks with composition varying from granite to

granodiorite and tonalite. Peralouminous rocks are present, as well as aluminosilicates.

6. Granulite-facies metapelites and migmatites, with alouminous parag-neiss and minor metabasites and metacarbonatic rocks. In the upper part, the granulite rocks show an overprint under amphibolite-facies conditions.

In some of the simulations (case F and G and Appendix C, Fig. C.1), we tested the rheological effect that the presence of mafic rocks can exert on the basement. This has been done by adopting a mineral assemblage for the middle and lower crust composed of gabbro for a volume percentage up to 35% vol., and the remaining volume constituted by the lithologies described above.

Appendix B. Procedure followed to develop the model

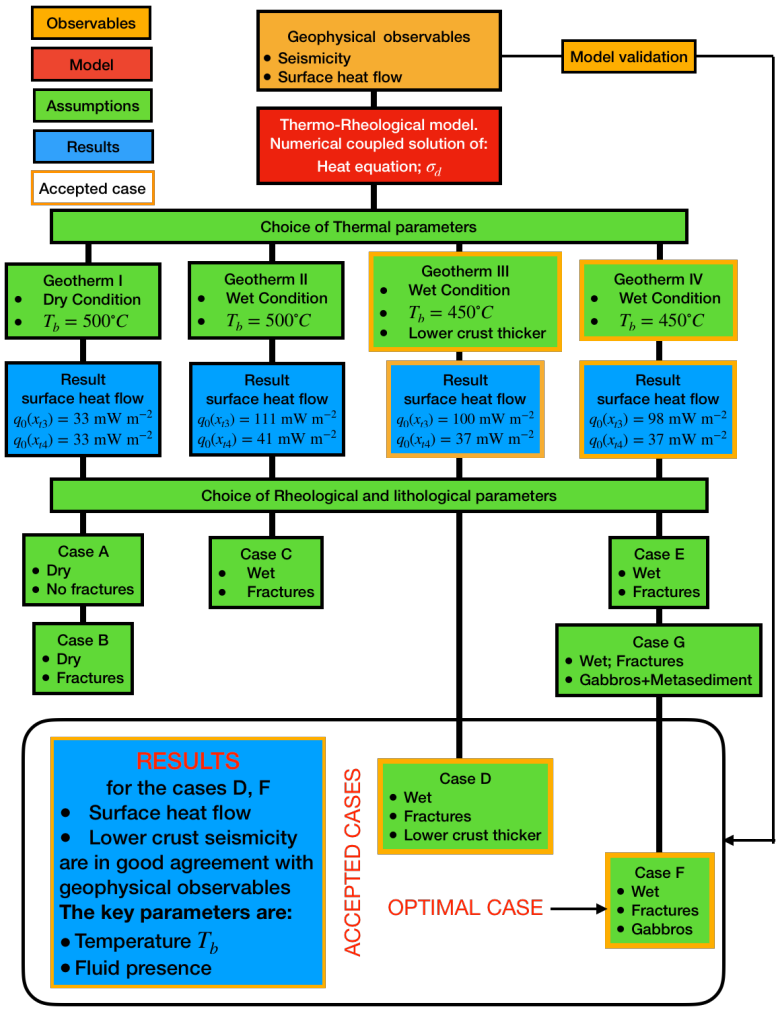

Figure B.1: Flow chart summarizing the procedure followed to develop the model.

Appendix C. Crustal rheology $R_h(x, z)$

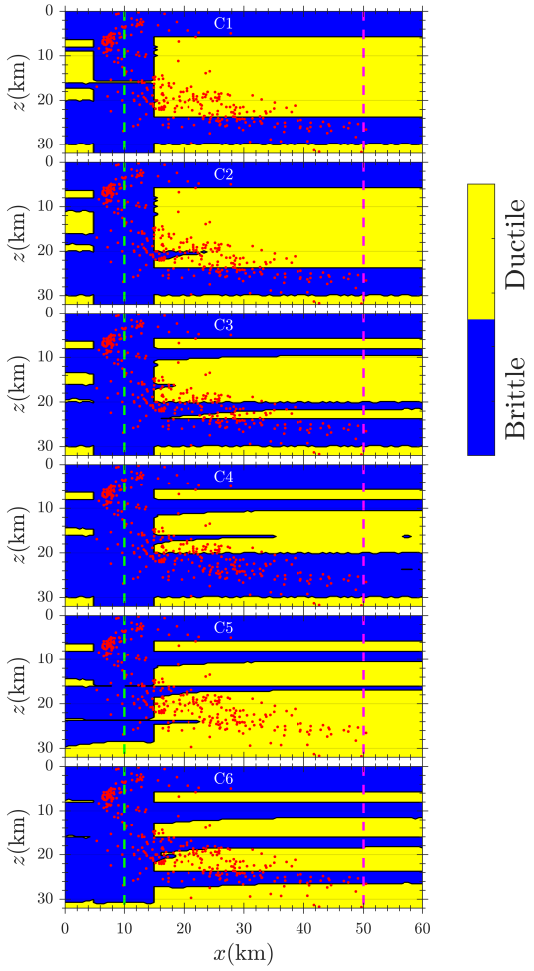

Figure C.1: Crustal rheology $R_h(x, z)$ in addition to the cases shown in Figs. 3-6 in the main text. Mafic material is intruded in the entire crystalline basement for different volume percentages: C1 10%, C2 20%, C3 30%, C4-C6 35%. For C5 and C6 dry condition is considered with $\lambda = 0.4$ in the entire crust. In C6 a strain rate $\dot{\varepsilon} = 10^{-13}$ s^{-1} is adopted. All other parameters are given in Tables 1, 2.